

Global view of inner magnetosphere composition during storm time

R. Ilie,¹ R. M. Skoug,¹ P. Valek,² H. O. Funsten,¹ and A. Gloer³

Received 2 November 2012; revised 4 October 2013; accepted 16 October 2013; published 18 November 2013.

[1] Plasma dynamics in the inner magnetosphere are greatly affected by variations in the ion composition. The ratio of hydrogen to oxygen has been shown to be highly dependent on geomagnetic activity. To investigate this dependence, we examine the timing of the injection and subsequent evolution of O^+ in the ring current during the storm of 6 August 2011 as observed by Two Wide-angle Imaging Neutral-atom Spectrometers (TWINS) instruments. To help interpret magnetospheric evolution using the global O Energetic Neutral Atom (ENA) emission measured by TWINS, we have employed a multidomain modeling of the global magnetosphere using the Space Weather Modeling Framework. TWINS Energetic Neutral Atom (ENA) imagers have the capability to distinguish between H and O emission and thus the major ion constituents of the ring current. Global composition measurements from TWINS spacecraft show intensifications of the oxygen ENA emission and thus an increase in the transport of ionospheric oxygen into the ring current that occur during the main phase of the storm. Both the observations and the simulation suggests that the peak in O ENA emission is correlated with the substorm injections that occurred during this time. The model also shows a very dynamic magnetosphere that allows for loss of oxygen from the Earth-magnetosphere system through plasmoids capable of transporting oxygen down the tail throughout the magnetic storm. This can possibly be a predominant pathway for loss of oxygen from the magnetosphere.

Citation: Ilie, R., R. M. Skoug, P. Valek, H. O. Funsten, and A. Gloer (2013), Global view of inner magnetosphere composition during storm time, *J. Geophys. Res. Space Physics*, 118, 7074–7084, doi:10.1002/2012JA018468.

1. Introduction

[2] The ionosphere and solar wind serve as the plasma boundaries of the magnetosphere and thus its source of both mass and energy. It is well-accepted that the ionospheric plasma is the main source of the plasmasphere [e.g., *Shelley et al.*, 1972, 1974; *Cladis and Francis*, 1985; *Cladis*, 1988; *Horwitz et al.*, 1990]. However, the ionospheric contribution to the plasma sheet and ring current, and in particular the physical mechanisms that control its entry and evolution, is still unknown. While the provenance of H^+ in the magnetosphere is usually ambiguous because it is the major component of both the solar wind and ionosphere, O^+ is predominantly of ionospheric origin and can be used to trace the transport and fate of ionospheric plasma in the magnetosphere. For example, several studies [see *Denton et al.*, 2005, and references therein] identify O^+ , and thus ionospheric plasma, in the plasma sheet.

[3] The plasma sheet is the source of high-energy plasma injected into the inner magnetosphere by strong magnetospheric convection during magnetic substorms and storms, considered to be one of the main mechanism responsible for the ring current enhancement during times of high geomagnetic activity. Plasma sheet density has a direct influence on the strength of the ring current [e.g., *Thomsen et al.*, 1998; *Kozyra et al.*, 1998] and is highly dependent on solar cycle [*Denton et al.*, 2005]. Ion composition in the magnetosphere is found to be dependent on the solar cycle as well [*Young et al.*, 1982].

[4] For many years, the solar wind has been believed to be a significant and effective source for the magnetospheric plasma. However, the entry mechanisms as well as the transport and acceleration processes acting on solar wind particles are still not well understood.

[5] On the other hand, *Chappell et al.* [1987], based on ionospheric outflow observations, hinted that the ionosphere alone is able to supply all magnetospheric plasma under any geomagnetic condition. The potential of the ionosphere to act as a source of magnetospheric plasma is the same as that of the solar wind and is limited as well to several transport and acceleration processes. Although there is controversy whether the dayside cleft or the auroral region are the dominant contributors to the ionospheric outflow, both are significant O^+ ion sources [*Yeh and Foster*, 1990; *Horwitz et al.*, 1992; *Lu et al.*, 1992; *Wing Ho et al.*, 1994]. It has been suggested that different magnetospheric conditions are regulated by different ionospheric outflow regions [*Daglis and Axford*, 1996]. Nevertheless, ion outflow is

¹Los Alamos National Laboratory, Los Alamos, New Mexico, USA.

²Southwest Research Institute, San Antonio, Texas, USA.

³NASA/GSFC, Greenbelt, Maryland, USA.

Corresponding author: R. Ilie, Los Alamos National Laboratory, Alamos, NM 87545, USA. (rilie@lanl.gov)

© 2013 The Authors. *Journal of Geophysical Research: Space Physics* published by Wiley on behalf of the American Geophysical Union.

This is an open access article under the terms of the Creative Commons Attribution-NonCommercial-NoDerivs License, which permits use and distribution in any medium, provided the original work is properly cited, the use is non-commercial and no modifications or adaptations are made. 2169-9380/13/10.1002/2012JA018468

a comparatively low energy process, and the acceleration mechanisms that control energization of ionospheric ions from few eV to keV range are still not understood.

[6] The composition of the ring current depends strongly on magnetic and solar activity. The detailed composition of the ring current was first reported during the Active Magnetospheric Particle Tracer Explorers mission in the late 1980s during solar minimum [Gloeckler *et al.*, 1985], and it was inferred that protons are the dominant ion species in the quiet time ring current, with the contribution of ions heavier than protons being essentially negligible.

[7] Hamilton *et al.* [1988] studied the ring current composition during an intense magnetic storm. They found that O^+ is the dominant ion, in terms of energy density, throughout the main phase of that particular storm and suggested that ionospheric ions can contribute up to 80% to the ring current energy density at the peak of the storm. Compositional information for the bulk of the ring current ions for the energy range between a few tens of keV to a few hundred keV was also made available from the Combined Release and Radiation Effects Satellite (CRRES) mission (1990–1991). Based on these observations, it was inferred [Daglis, 1997] that the O^+ content increases with increasing geomagnetic activity, i.e., larger storms display a larger O^+ contribution to the ring current population. However, based on CRRES observations, a saturation value for the energy density of O^+ has been suggested [Fu *et al.*, 2001].

[8] Delcourt and Sauvaud [1991] suggests that it is the ionospheric outflow that contributes significantly to the trapped energetic populations in the near-Earth region. GEOTAIL observations confirm the presence of oxygen even in the distant magnetotail, during flow reversal events [Christon *et al.*, 1994]. Increased oxygen to hydrogen ratio in the distant magnetotail suggest that the observed oxygen ions are more efficiently accelerated than hydrogen ions during energetic ion enhancement events [Wilken *et al.*, 1995]. Moreover, using ENA imaging of O emission, during storm time substorm onsets, the oxygen abundance was shown to enhance in bursts [Mitchell *et al.*, 2003].

[9] Variations in the magnetospheric composition can have profound influence on plasma structures, including modification of temperature and the magnetic field configuration. As a result, it modifies the convection patterns inside the magnetosphere. Recent modeling efforts have further shown the importance of including oxygen in modeling the dynamics of magnetic storms. When included in global MHD simulations, ionospheric outflow drives a strong decrease in the *Dst* index as well as in the cross polar cap potential [Glocer *et al.*, 2009b], as compared to simulations that do not account for polar wind outflow into the magnetosphere. Moreover, the overall comparison of modeled magnetic field with in situ data shows significant improvement in the data-model comparison. Including outflow effects changes the overall composition into the inner magnetosphere leading to changes in the ring current energy density [Welling *et al.*, 2011].

[10] A global view of the magnetospheric composition was previously possible only from the numerical simulation perspective. We present here for the first time a global view of the magnetospheric composition during 5 August 2011 magnetic storm from both numerical and TWINS perspective.

[11] This study uses simulations with the Space Weather Modeling Framework (SWMF) together with first composition measurements from TWINS imagers to investigate the global dynamics of oxygen and hydrogen ions throughout the storm time magnetosphere. We employ self-consistent simulations of the global magnetosphere with the multifluid MHD version of Block Adaptive Tree Solar-wind-type Roe Upwind Scheme (BATS-R-US) coupled with models for the ring current, ionospheric electrodynamics, and physics based ionospheric outflow. The model setup is described in section 2. The methodology used to extract the composition information from TWINS measurements is described in section 3. This first direct comparison of the model-derived oxygen and hydrogen ENA fluxes with mass-separated ENA images from TWINS is described in section 4. Section 5 shows the GEOTAIL comparison with the SWMF magnetic field results while section 6 presents a summary of the main findings of this study.

2. The Model

[12] In order to gain a better understanding of the physical processes that control the transport and loss of oxygen ions in the inner magnetosphere, complementary to the TWINS observations, numerical simulations with Space Weather Modeling Framework (SWMF) are employed. The simulation presented here involves five modules within the SWMF that are used to simulate the global magnetosphere (GM), the ionosphere electrodynamics (IE), the inner magnetosphere (IM), the polar wind (PW) outflow, and the thermosphere and ionosphere (TI).

[13] The Space Weather Modeling Framework is a robust, high-performance, and heavily tested numerical tool which integrates numerical models from numerous physics domains and can be customized to self-consistently simulate physical processes and coupled domains from the solar surface to the upper atmosphere of the Earth [Tóth *et al.*, 2005, 2007, 2012a]. Each domain can be represented with alternative physics models, and the coupling of these modules makes the SWMF a unique and powerful tool in simulating the dynamic evolution and interactive physical dependencies within and between coupled systems of the space environment. SWMF has been extensively used for scientific studies of geospace by many authors, e.g., Tóth *et al.* [2005, 2007], Zhang *et al.* [2007], Yu and Ridley [2009], and Ilie *et al.* [2010a, 2010b].

[14] The GM component is based on the Block Adaptive Tree Solar-wind-type Roe Upwind Scheme (BATS-R-US) global magnetohydrodynamic (MHD) model [Powell *et al.*, 1999; Tóth *et al.*, 2006] and describes the magnetic field and plasma properties in the outer magnetosphere, encompassing the bow shock, the magnetopause, and the magnetotail of the planet. The GM component is driven by solar wind observations from the ACE satellite orbiting at the Lagrange 1 point around the Sun-Earth line. The version of the BATS-R-US model used for this study solves the multifluid magnetohydrodynamic equations [Glocer *et al.*, 2009c; Tóth *et al.*, 2012b], everywhere outside an inner boundary near Earth, taken here at $2.5 R_E$. The multifluid MHD version of BATS-R-US will enable us to follow each species within the simulation domain as a separate fluid and assess the relative

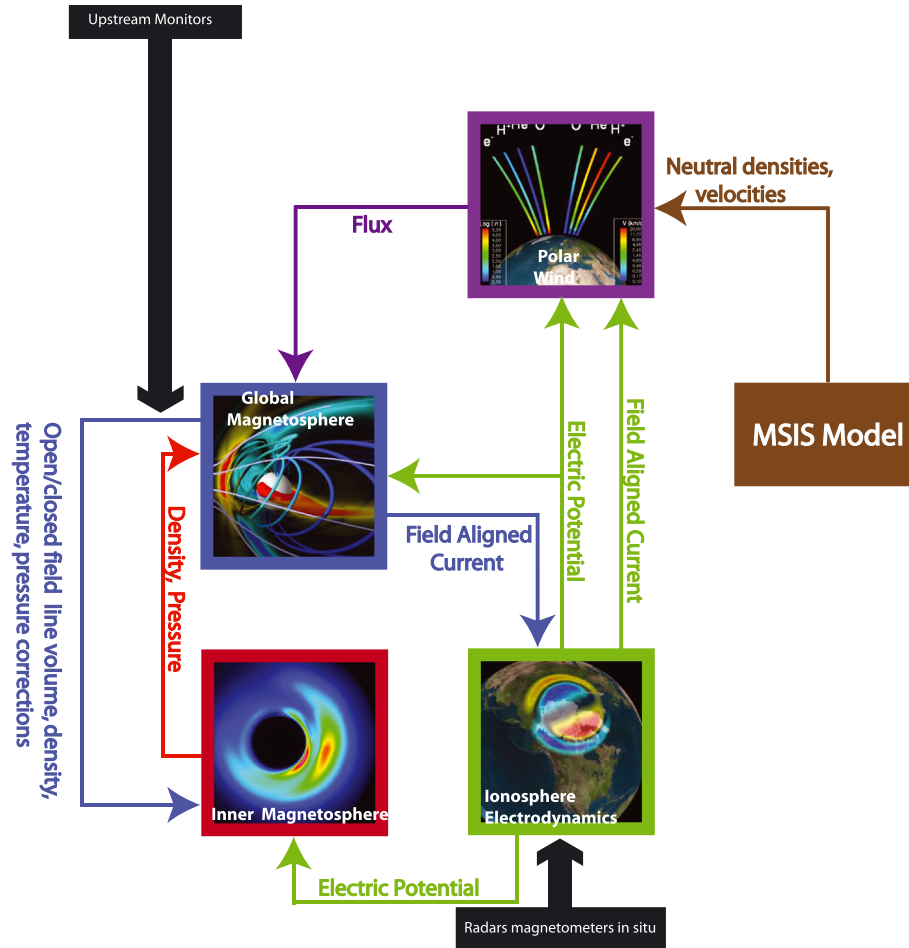


Figure 1. Coupling schematic of the module coupling within SWMF.

contribution of hydrogen and oxygen to the formation and decay of the ring current.

[15] The GM component couples to all the other modules. In the regions close to the Earth, where the grid overlaps with that of the Inner Magnetosphere component, the MHD results are self-consistently driven toward the IM results [De Zeeuw *et al.*, 2004; Glozer *et al.*, 2009a], while the flux tube volume and ionospheric footprints are passed through couplers to the IM component. The Rice Convection Model (RCM) [Harel *et al.*, 1981; De Zeeuw *et al.*, 2004] is the IM model used for this study. It represents the plasma population in terms of multiple isotropic fluids and calculates the dynamic behavior of the inner-magnetospheric particles in a region of the magnetic equatorial plane that extends from just inside the dayside magnetopause to the nightside inner plasma sheet. When coupled with BATS-R-US, the outer boundary is dynamic, following the boundary of the last closed field lines.

[16] Transfer of information from GM to IM is expedited by efficient ray-tracing algorithms in BATS-R-US, as described by De Zeeuw *et al.* [2004]. The GM domain provides the open/closed field line boundary and passes it to the IM module on each coupling to update the spatial boundary on a continuous basis. In turn, the IM computes the density and pressure along those closed field lines and feeds this information to GM in order to correct these values.

[17] The ionospheric electrodynamic (IE) component is based on an ionospheric model that combines an electric potential solver with a model of the electron precipitation [Ridley and Liemohn, 2002; Ridley *et al.*, 2004]. The field-aligned current strength and position are passed to the IE component from the GM component, which in turn returns the electric potential at the GM boundary. This value is converted to velocity at the inner boundary. IE also provides the electric potential to the IM component.

[18] The Polar Wind Outflow Model (PWOM) [Glozer *et al.*, 2007, 2009b, 2012] simulates the ionospheric outflow by calculating the vertical transport of O^+ , He^+ , and H^+ ions and electrons by solving the gyroscopic transport equations [Gombosi and Nagy, 1989] along a magnetic field line. The domain covers the gap region, a region of space that spans from the ionosphere (~ 1000 km) to the inner boundary of the global magnetospheric (GM) model ($2.5 R_E$). The resulting outflow flux from PWOM is used to set the inner boundary mass and radial velocity of the MHD model [Glozer *et al.*, 2009b]. Neutral densities, used to calculate losses and sources of different atomic and molecular species, are obtained from the Mass Spectrometer Incoherent Scatter empirical model [Hedin, 1987, 1992] (TI) component. An illustration of the SWMF modules and their coupling is presented in Figure 1. This is the first time we are carrying out a numerical experiment in this setup.

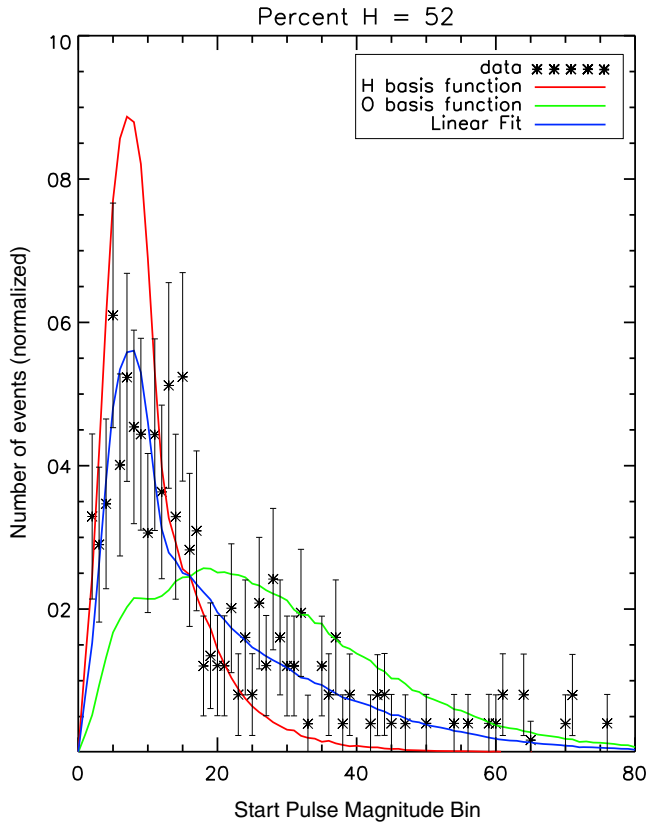


Figure 2. Example for composition fitting procedure, normalized pulse height distribution of stop counts. The red line shows the H basis function from calibration data, the green line shows the O basis function from calibration data, the stars show the TWINS observation that contains both H and O ENA while the black line shows the linear fit as a combination of the red and green line as described by equation (1).

3. Extracting Composition Information From TWINS ENA

[19] The general state of the magnetosphere at any given time is highly complex and unknown; therefore, global imaging is crucial for a global view of the magnetospheric structure and dynamics. The TWINS mission [McComas *et al.*, 2009] is a NASA Explorer Mission-of-Opportunity that includes two identical cross-calibrated Energetic Neutral Atom (ENA) imagers flown aboard two separate spacecraft in Molniya orbits (inclination of 63° , orbital period of 12 h, and apogee $\sim 7.2 R_E$) to image the inner magnetosphere. TWINS is the first mission to stereoscopically image ENA emission from the Earth's magnetosphere. The TWINS ENA sensors image neutral atoms at very high angular resolution ($\sim 1^\circ$) with $\Delta E/E \leq 1.0$ for H atoms. Full images are taken typically every 72 s over an energy range from ≤ 1 keV/amu up to ~ 100 keV/amu. See McComas *et al.* [2012, Appendix A] for a full description of how the ENAs are processed to generate images.

[20] Both H^+ and O^+ in the magnetosphere charge exchange efficiently with the exosphere and upper atmospheric neutrals producing H and O ENAs.

[21] An important component of the TWINS science objective is to better understand the differences in the dynamics and transport of H^+ and O^+ . Mass separation of the ENA species is achieved through statistical analysis of pulse height information. TWINS utilizes foil-based time-of-flight, in which a start pulse is generated by secondary electron emission from the back surface of an ultra thin foil and a stop pulse is registered by detection of the ENA. This measurement, coupled with position-sensing of the detected locations of both the start and stop pulses, provides measurement of ENA velocity (speed and direction).

[22] The ENA-induced secondary electron yield from the exit surface of the foil is primarily dependent on ion atomic number and secondarily on ion speed [Ritzau and Baragiola, 1998], with O^+ producing, on average, substantially more secondary electrons than H^+ at the same speed and therefore generating, on average, a significantly higher pulse magnitude in the TWINS detector. However, the number of secondary electrons produced from a single ENA follows a Poisson distribution [Gruntman *et al.*, 1990] that, when combined with the probability that each of the electrons contributes to the measured pulse, is sufficiently wide that individual ENAs cannot be uniquely identified as H^+ or O^+ . Therefore, species identification requires statistical analysis of the pulse height distribution of an ensemble of detected ENAs.

[23] The start pulse height distributions PH_H and PH_O for incident H and O ENAs, respectively, were obtained as a function of incident energy during TWINS calibration. The start pulse height distribution PH of TWINS ENA observations collected over a period of time is therefore a linear combination of the pristine H and O pulse height distributions according to

$$PH = \alpha \cdot PH_H + (1 - \alpha) \cdot PH_O \quad (1)$$

where α is the derived fraction of H ENA events and $1 - \alpha$ is the derived fraction of detected O events. Importantly, α is not the relative fraction of incident H ENA flux because equation (1) applies only to detected counts and the detection probabilities of H and O are different; the relative detection probabilities, derived during TWINS calibration, are then applied to α to derive the relative H and O abundances as well as H and O ENA fluxes.

[24] To illustrate our method, Figure 2 shows an example of the linear fit for a specific pixel in one image. Red and green lines show the H and O basis functions as obtained from calibration while the stars show the TWINS data. Error bars are shown for the observations. The blue line represents the linear fit between the red and green line, and for this particular case, the α parameter was found to be 52 (with a reduced χ^2 of 0.15), which corresponds to 52% hydrogen. It is worth mentioning that our methodology assumes that there are only two species, hydrogen and oxygen, that populate the inner magnetosphere. This, however, is a reasonable assumption since other candidates, like helium, have been found in lower abundances, based on the charge exchange cross section of He^+ ions on geocoronal hydrogen [Phaneuf *et al.*, 1987]. For more details on the methodology, see Valek *et al.* [2013].

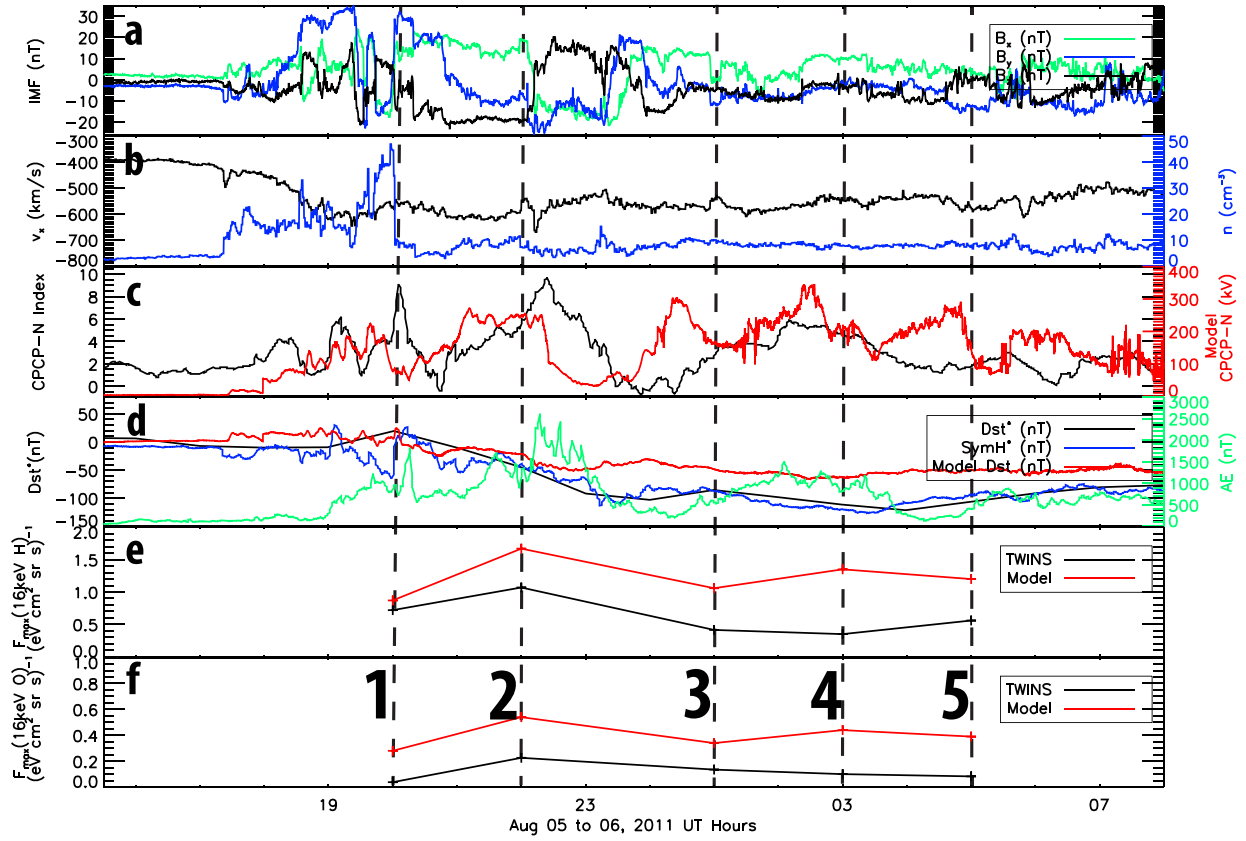


Figure 3. (a) Interplanetary magnetic field components (B_x = green line, B_y = blue line, and B_z = black line). (b) Solar wind density (blue line) and the earthward component of the solar wind velocity (black line). (c) Cross polar cap potential from Thule (black line) and the synthetic Cross Polar Cap Potential (CPCP) (red line). (d) Evolutionary tracks of the Dst^* (black line), Sym-H (blue line), and AE (green line) indices. (e) Maximum value of the 16 keV H ENA flux as observed by TWINS (black line) and derived from the SWMF simulation (red line). (f) Maximum value of the 16 keV O ENA flux as observed by TWINS (black line) and derived from the SWMF simulation (red line).

4. Results

4.1. The 5 August 2011 Event

[25] The 5–6 August 2011 event was one of the larger Coronal Mass Ejection (CME)-driven storms that occurred at the end of the prolonged solar minimum leading into solar cycle 24 and was selected based on the availability of TWINS composition data. During this storm, the pressure-corrected Dst^* index went down to -113 nT while the SYM-H index reached a minimum of -126 nT.

[26] Figure 3a presents the interplanetary magnetic field components (B_x = green line, B_y = blue line, and B_z = black line) as measured by the ACE spacecraft during this time, followed by the solar wind density (blue line) and the earthward component v_x of the solar wind velocity (black line) in Figure 3b.

[27] At 17:20 UT the solar wind density suddenly doubles relative to its value during quiet time period and continues to increase during the initial phase of the storm, reaching a maximum of 47 cm^{-3} , only to drop sharply to $\sim 8 \text{ cm}^{-3}$ at 20:00 UT. This time marks the beginning of the storm main phase, when the interplanetary magnetic field (IMF) B_z turns southward and remains negative for the next 2 h. The solar wind speed v_x starts to increase at the same time as the

sudden density increase and remains elevated for the whole storm time interval.

[28] The cross polar cap index (PCI) from Thule magnetometer is presented as the black line in Figure 3c while the modeled Cross Polar Cap Potential (CPCP) is shown in red. Thule PCI has been shown to be highly correlated with the cross polar cap potential [Lukianova *et al.*, 2002; Fiori *et al.*, 2009] and for this event is the only observationally based proxy for the ionospheric convection that was available.

[29] We note the peak in the cross polar cap potential index at the time the IMF B_z turns southward. This index decreases for the next hour and then ramps up during the period of negative B_z , reaching its second peak at about 22:20 on 5 August. Its simulated counterpart roughly follows the behavior of the CPCP index; however, we note a time lag between the two quantities on the order of minutes.

4.2. TWINS and SWMF

[30] Figure 3d presents the pressure-corrected Dst^* (black line) and Sym-H index (blue line) during this storm interval. Similar to the Dst^* index, the Sym-H geomagnetic index is also an indicator of geomagnetic activity, but it has the advantage that it has 1 min temporal resolution, compared to 1 h for Dst^* . The Dst^* and Sym-H indices are not only

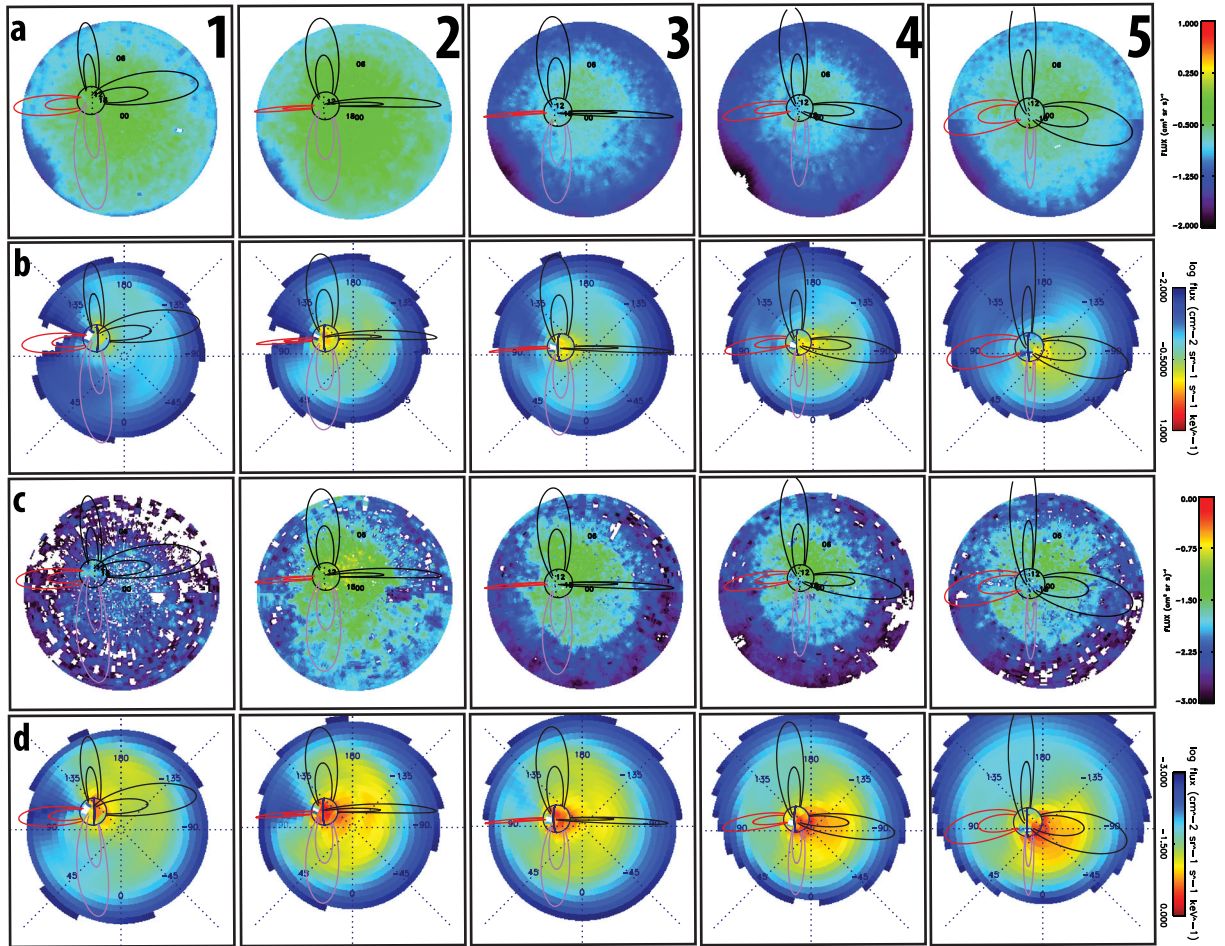


Figure 4. (a) TWINS 16 keV H ENA fluxes extracted at 5 times during the storm time. (b) Synthetic TWINS 16 keV H ENA fluxes extracted at 5 times during the storm time. (c) TWINS 16 keV O ENA fluxes extracted at 5 times during the storm time. (d) Synthetic TWINS 16 keV O ENA fluxes extracted at 5 times during the storm time. (Figures 4a–4d) The scale is logarithmic and the same for observed and simulated fluxes.

different in time resolution but also in the number and location of magnetometer stations used and the methods employed to calculate and convolve station data into a final index. These systematic differences contribute to the differences between the two observed indices. The red line shows the synthetic Dst index which was calculated by solving the Biot-Savart integral for all the electric currents encompassed by the BATS-R-US simulation domain from the inner boundary outward, and taking the magnetic field disturbance along the z axis. We note that the simulated disturbance index closely follows the observed one throughout the main phase of the storm but it does not reach as low values as the observed Dst^* . Even though both Sym-H and the simulated counterpart function as proxies for the strength of the geomagnetic disturbance, the methodology to obtain them differ significantly (please note that at times Dst and Sym-H can differ by as much as 90 nT). However, the correlation coefficient between the simulated Sym-H and the observed one is of 0.86 while the correlation coefficient between the two observationally based indices, Dst^* and Sym-H, is 0.91. This implies that the model and its underlying physics

represents the storm evolution reasonably well for the duration of the storm.

[31] In the same panel we also present the AE index (green line), which is an indicator of substorm activity [Davis and Sugiura, 1966]. The AE index shows a first peak after 20:00 UT on 5 August and a second one during the main phase of the storm, indicating substorm injections occurred during this magnetic storm.

[32] Both TWINS spacecraft observed the magnetosphere during this storm interval. We extracted data from five distinct times throughout the event to correspond to quiet, main, and recovery phases of the storm. The time stamps are denoted by vertical dashed lines in Figures 3a–3f. From left to right, the first time stamp corresponds to quiet time, followed by 3 times during the storm main phase, and 1 during the recovery phase. For the first 2 times, TWINS 1 was probing the magnetosphere, while at the last 3 selected times, the ENA observations were made by TWINS 2.

[33] Figure 4a shows the mass-separated 16 keV H ENA fluxes at the aforementioned times. The images are created from 1 h acquisition time for each data image. Earth and the

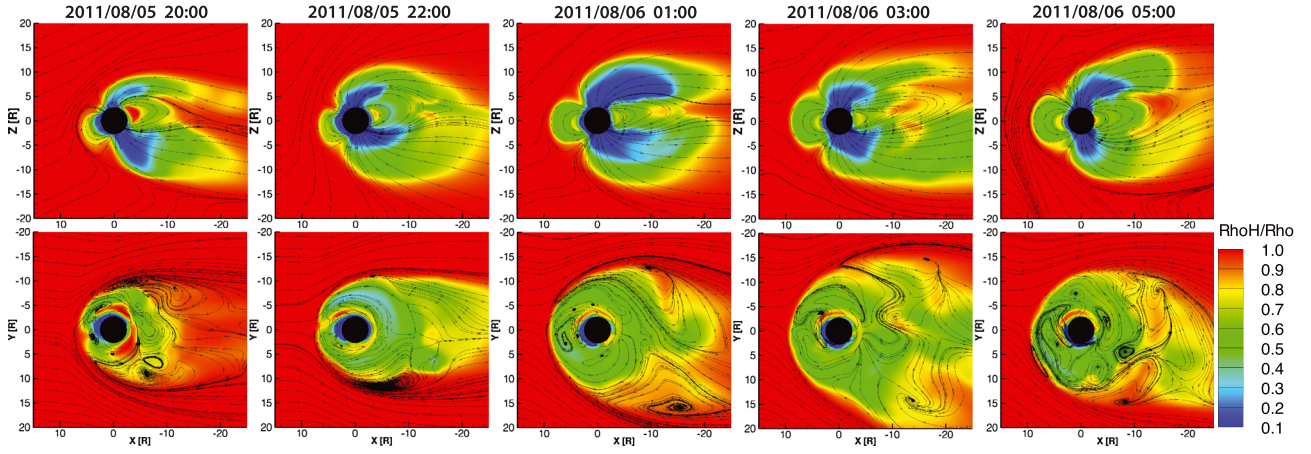


Figure 5. (top row) The simulation results showing the configurations (magnetic field) and the content (fraction of hydrogen number density) of the magnetosphere in the $y = 0$ plane. (bottom row) The configurations (convection patterns) and the content (fraction of hydrogen) of the magnetosphere in the $z = 0$ plane. The color changes from 100% H (red) to 100% O (blue).

dipole field lines at $L = 4$ and $L = 8$ are drawn at four magnetic local times: noon (red line), dusk (magenta line), and midnight and dawn (black lines). We note that the highest emissions are seen during the early main phase while the H flux decrease in the first part of the recovery phase, as more hydrogen ions are injected into the inner magnetosphere in the main phase and are lost during the recovery.

[34] Figure 4c presents snapshots of the 16 keV oxygen ENA fluxes during the same times as previously described. The strongest oxygen emissions are observed during the early main phase on 5 August 2011 at 22:00 UT. This is a time when the *AE* index (Figure 3d, green line) is increasing, signaling the onset of a substorm. It has been shown that the abundance ratio of hydrogen to oxygen decreases with time during a substorm, with the magnetospheric composition shifting from predominantly H^+ to predominantly O^+ [Gazey *et al.*, 1996]. Moreover, even though the total ENA emissions become weaker during the recovery phase, the presence of oxygen is more noticeable than in the prestorm time.

[35] Simulated hydrogen (oxygen) ENA fluxes at the locations of the TWINS spacecraft are shown in Figure 4b (Figure 4d). These ENA images were constructed from the simulated ring current differential ion fluxes by performing line-of-sight integration of the ENA flux from the TWINS position to the boundary of the simulation domain:

$$j_{\text{ENA}} = \int j_{\text{ion}} \sigma_{\text{CE}} n_H dl \quad (2)$$

where j_{ion} corresponds to the H^+ or O^+ ion differential flux from the inner magnetosphere model, σ_{CE} represents the charge exchange cross section of H^+ or O^+ ion with geocoronal neutral H [Lindsay and Stebbings, 2005], and n_H is the geocoronal neutral hydrogen density derived from the Rairden *et al.* [1986] geocoronal model. This model assumes a spherically symmetric neutral hydrogen density distribution, yet it has been previously shown that the asymmetries in the geocoronal density distribution play an important role in producing an accurate representation of the storm time

ring current [Ilie *et al.*, 2012]. However, for the purpose of this study and for consistency with RCM we use the Rairden *et al.* [1986] geocoronal density model.

[36] Figures 3e and 3f show the evolutionary tracks of the maximum 16 keV H (O) flux during this event, as seen by TWINS spacecrafts (black line) and extracted from the simulation (red line). This quantity provides a global qualitative overview of the maximum ENA production in the ring current. We use here the maximum value of the ENA flux as a proxy for the time when the charge exchange losses are the highest. Both the model and the observations show the highest hydrogen and oxygen emissions during the main phase of the storm, right after the substorm occurrence (5 April 2011 at 22:00 UT). During the initial phase of the storm (5 August 2011 at 20:00 UT) the hydrogen emissions are the strongest in the morning/postmidnight sector and extend past $8 R_E$. As the storm progresses, the location of the brightest hydrogen ENA emission moves toward the dayside.

[37] The postmidnight enhancements are due to skewed electric fields that strongly influence the low energy ENA [C:son Brandt *et al.*, 2002]. The high-energy particles experience stronger gradient curvature drifts and are less affected by this electric fields leading to a peak in the ring current pressure in the premidnight sector. Our findings are consistent with those of Buzulukova *et al.* [2010].

[38] The modeled oxygen emissions are also strongest during the middle main phase and can be seen on the entire nightside. As the storm progresses, the location of the brightest ENA oxygen emission move in local time from nightside toward the dusk. O emission becomes weaker during the early recovery phase only to increase again toward the late recovery. This bright emission is observed by the TWINS spacecraft. There are few discrepancies between the model and the observations. Pitch angle isotropy is one limitation of the inner magnetosphere model. However, the TWINS viewing perspective is considerably dependent on the pitch angle distribution [Zheng *et al.*, 2008]. Moreover, TWINS observations [Goldstein *et al.*, 2012] reveal a global dawn-dusk asymmetry favoring pitch angle anisotropy on the duskside.

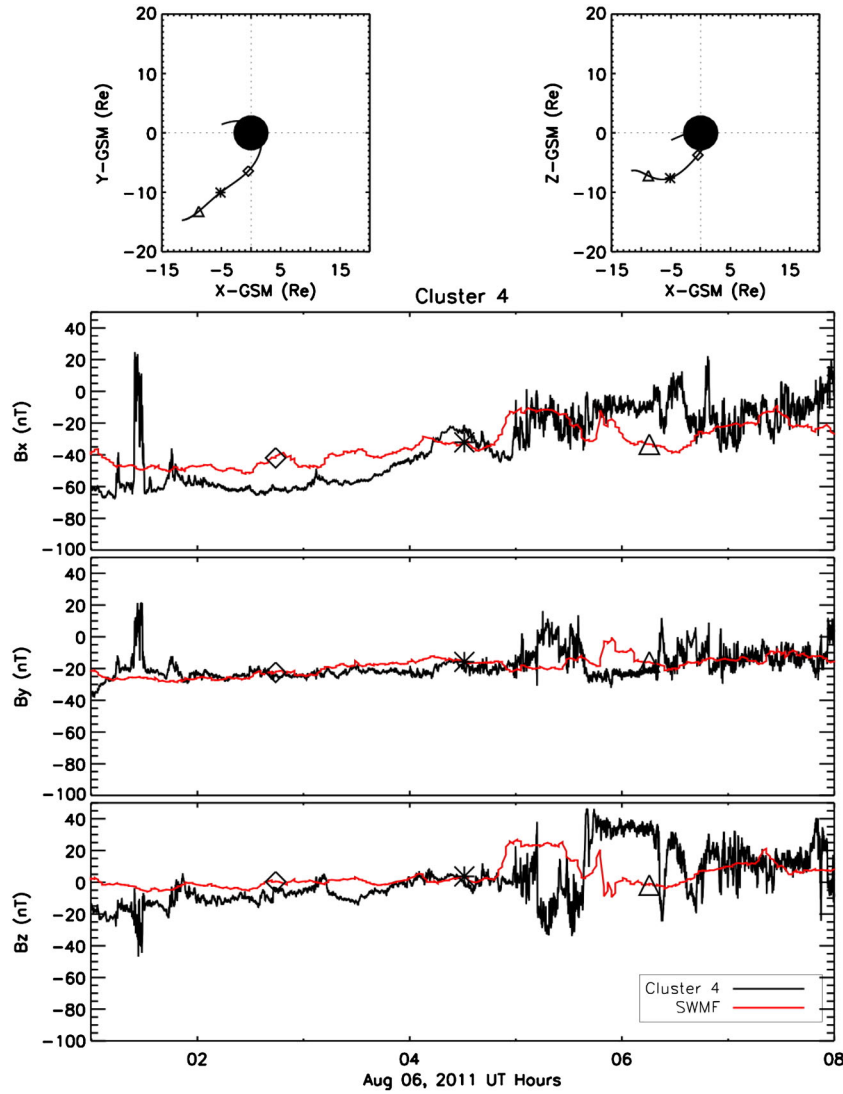


Figure 6. Data-model comparison for the 6 August 2011, showing (top row) the Cluster 4 position in the $Y, Z = 0$ planes, followed the magnetic field components as measured by the satellite (black lines) and predicted by the model (red lines). The green diamond, star, and triangle are used to show the satellite position and progression during the time interval presented here.

Therefore, the pitch angle anisotropy can possibly account for the differences in the modeled versus the observed ENA fluxes.

[39] Figure 5 (top row) shows the modeled magnetic field (black lines) and the content of the magnetosphere in terms of the fraction of hydrogen number density (color contours) in the noon-midnight meridional plane while Figure 5 (bottom row) shows the convection patterns (black lines) and the magnetospheric content in the $z = 0$ plane. The snapshots are extracted at the same time as the ENA observations in Figure 4, starting during quiet time and progressing throughout the storm. A black disk with radius of $2.5 R_E$ denotes the inner boundary for this simulation.

[40] Figure 5 reveals a very dynamic magnetosphere with rapid changes in composition. Plasma of solar wind origin (hydrogen only) dominates the magnetosphere during the prestorm period. However, as the storm progresses,

ionospheric outflow of oxygen starts to fill up the inner and outer magnetosphere and becomes the major constituent of the plasma sheet population during the disturbed time. Mixing of the solar wind plasma is observed along the magnetopause but solar wind plasma does not penetrate deeply into the magnetosphere. Moreover, oxygen plasmoids are transported down the tail, thus distributing oxygen of ionospheric origin far down the tail. These results suggest that oxygen transport down the tail is the primary loss pathway of oxygen from the Earth's magnetosphere system. However, this feature is only seen in the details of the simulation as the data is limited to $x \leq 12 R_E$. Moreover, the TWINS observations mentioned here are not intended to validate the model, but rather, we make use of the SWMF to corroborate and validate the methodology for extracting the oxygen information from the measurements of ENA fluxes by the TWINS imagers.

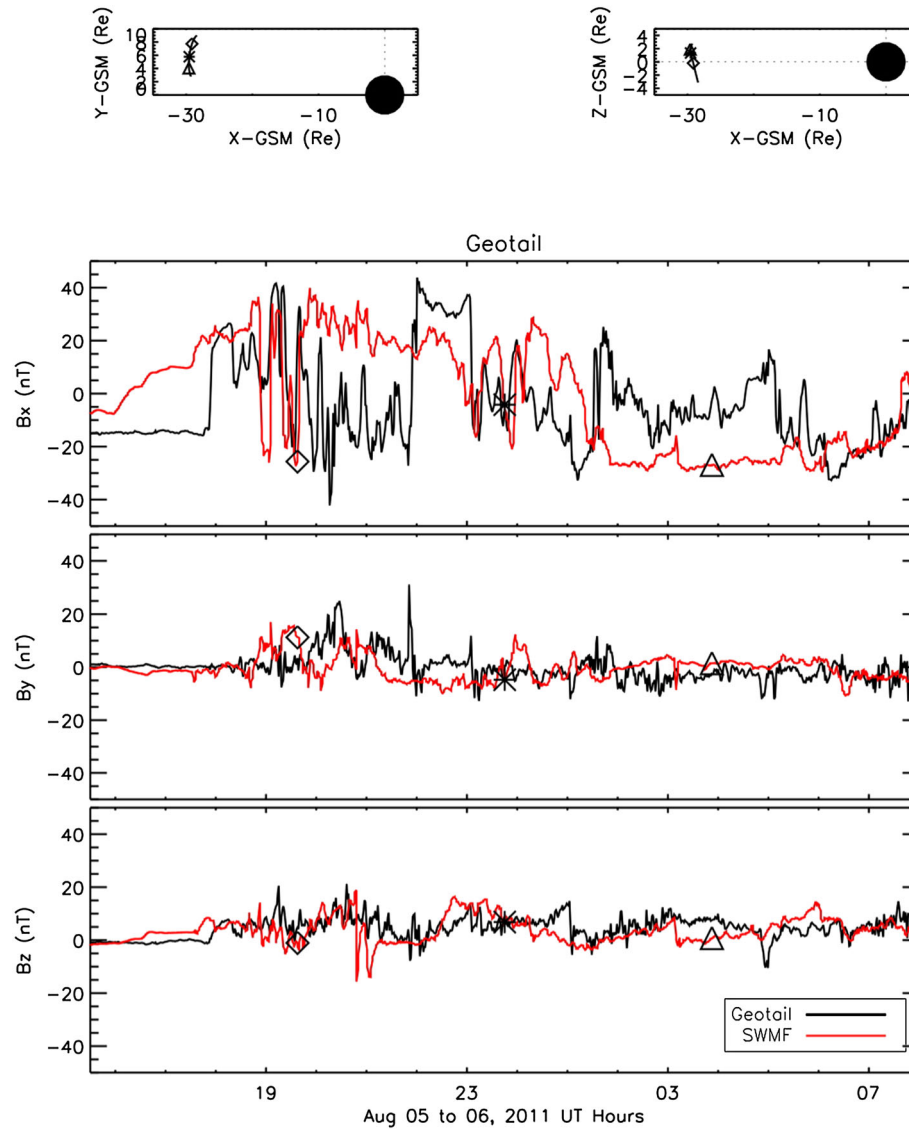


Figure 7. Data-model comparison for the 5–6 August 2011, showing (top row) the Geotail position in the $Y, Z = 0$ planes, followed the magnetic field components as measured by the satellite (black lines) and predicted by the model (red lines). The green diamond, star, and triangle are used to show the satellite position and progression during the time interval presented here.

5. Model Validation

[41] During the last day of the event, the Cluster 4 satellite passed through the nightside magnetosphere. As a way to validate the magnetic field model results we compare with the in situ magnetic field observations from the Cluster 4 spacecraft. The satellite position is shown in Figure 6 (top row) and magnetic field components are presented in the following three rows. The black lines represent in situ measurements from the Cluster 4 spacecraft while the red lines show the simulated values for the same quantities. The comparison between the observations and the simulation results suggests that the magnetic field is predicted very well by the model throughout this time period, with the best agreement happening during the time the satellite is on the nightside of the magnetosphere. Similarly, Figure 7 presents magnetic field measurements from the Geotail satellite and the corresponding numerical solution for the same parameters,

extracted from the model output at the satellite location. The agreement between the data and the model is best for B_y and B_z . One of the possible factors responsible for the disagreement between the modeled and observed quantities is that Geotail is farther from the Earth during this time, and in this region, the resolution in the computational domain is coarser. Other magnetospheric observations during this storm were limited. Only Geotail and Cluster measurements were available.

6. Conclusions

[42] New composition information from the TWINS spacecraft together with the state-of-the-art multifluid version of BATS-R-US coupled to an ionospheric outflow model were employed to investigate the magnetospheric composition during the storm of 5 August 2011. This event

was one of the largest that has occurred since the TWINS mission was launched.

[43] Oxygen observations from the TWINS spacecraft show intensifications of the oxygen ENA emission and thus increased transport of ionospheric oxygen into the ring current that occurs during the main phase of the storm. Moreover, there is evidence that the peak in oxygen ENA emissions is correlated with the substorm injections that occurred during this time. The highest hydrogen ENA fluxes are seen during the early main phase and decrease in the first part of the recovery phase, as more hydrogen ions make their way into the inner magnetosphere in the main phase of the storm.

[44] Simulations with the Space Weather Modeling Framework also show the increased presence of oxygen in the magnetosphere. The model suggests that the peak in both the hydrogen and oxygen emissions occurs immediately following the first substorm intensification, as suggested by the peak in the *AE* index. The strongest hydrogen emissions are seen in the morning/postmidnight sector and extend past 8 R_E . As the storm progresses, the peak in the hydrogen ENA fluxes moves toward the dayside and the spatial extent is decreasing. The modeled oxygen emissions are also strongest on the nightside and mostly during the middle main phase but move in local time, from nightside toward dusk and become weaker during the early recovery phase.

[45] The model also shows a very dynamic magnetosphere that allows for rapid changes in its composition. Moreover, plasmoids of oxygen are being transported down the tail throughout the magnetic storm and represents a predominant pathway for loss of oxygen from the Earth-magnetosphere system. Comparison of magnetic field measurements from Cluster 4 and Geotail satellites to the predicted values from the SWMF shows good agreement between the two for this storm interval suggesting the physics represented in the model reasonably represents that of the physical system.

[46] **Acknowledgments.** Work at Los Alamos was performed under the auspices of the U.S. Department of Energy with financial support from the NSF grant NSF AGS 1027008 and the NASA TWINS project. We gratefully acknowledge Natasha Buzulukova and Mei-Ching Fok from NASA Goddard for providing the ENA tool as well as the whole SWMF team at University of Michigan. We would like to thank Sorin Zaharia from Los Alamos National Laboratory for valuable comments.

[47] Masaki Fujimoto thanks the reviewers for their assistance in evaluating this paper.

References

- Buzulukova, N., M.-C. Fok, J. Goldstein, P. Valek, D. J. McComas, and P. C. Brandt (2010), Ring current dynamics in moderate and strong storms: Comparative analysis of TWINS and IMAGE/HENA data with the Comprehensive Ring Current Model, *J. Geophys. Res.*, **115**, A12234, doi:10.1029/2010JA015292.
- Chappell, C. R., T. E. Moore, and J. H. Waite Jr. (1987), The ionosphere as a fully adequate source of plasma for the Earth's magnetosphere, *J. Geophys. Res.*, **92**, 5896–5910, doi:10.1029/JA092iA06p05896.
- Christon, S. P., et al. (1994), Energetic atomic and molecular ions of ionospheric origin observed in distant magnetotail flow-reversal events, *Geophys. Res. Lett.*, **21**, 3023–3026, doi:10.1029/94GL02095.
- Cladis, J. (1988), Transport of ionospheric ions in the magnetosphere: Theory and observations, *Adv. Space Res.*, **8**(8), 165–173, doi:10.1016/0273-1177(88)90283-9.
- Cladis, J. B., and W. E. Francis (1985), The polar ionosphere as a source of the storm time ring current, *J. Geophys. Res.*, **90**(A4), 3465–3473, doi:10.1029/JA090iA04p03465.
- Cson Brandt, P., S. Ohtani, D. G. Mitchell, M.-C. Fok, E. C. Roelof, and R. Demajistre (2002), Global ENA observations of the storm mainphase ring current: Implications for skewed electric fields in the inner magnetosphere, *Geophys. Res. Lett.*, **29**(20), 1954, doi:10.1029/2002GL015160.
- Daglis, I. A. (1997), The role of magnetosphere-ionosphere coupling in magnetic storm dynamics, in *Magnetic Storms, Geophysical Monograph Series*, edited by B. T. Tsurutani et al., 107–116, vol. 98, AGU, Washington, D. C.
- Daglis, I. A., and W. I. Axford (1996), Fast ionospheric response to enhanced activity in geospace: Ion feeding of the inner magnetotail, *J. Geophys. Res.*, **101**, 5047–5066, doi:10.1029/95JA02592.
- Davis, T. N., and M. Sugiura (1966), Auroral electrojet activity index *AE* and its universal time variations, *J. Geophys. Res.*, **71**(3), 785–801.
- De Zeeuw, D. L., S. Sazykin, R. A. Wolf, T. I. Gombosi, A. J. Ridley, and G. Toth (2004), Coupling of a global MHD code and an inner magnetospheric model: Initial results, *J. Geophys. Res.*, **109**, A12219, doi:10.1029/2003JA010366.
- Delcourt, D. C., and J. A. Sauvaud (1991), A quantitative study of ion transport during substorms, *Adv. Space Res.*, **11**, 171–175, doi:10.1016/0273-1177(91)90029-J.
- Denton, M. H., M. F. Thomsen, H. Korth, S. Lynch, J. C. Zhang, and M. W. Liemohn (2005), Bulk plasma properties at geosynchronous orbit, *J. Geophys. Res.*, **110**, A07223, doi:10.1029/2004JA010861.
- Fiori, R. A. D., A. V. Koustov, D. Boteler, and R. A. Makarevich (2009), PCN magnetic index and average convection velocity in the polar cap inferred from SuperDARN radar measurements, *J. Geophys. Res.*, **114**, A07225, doi:10.1029/2008JA013964.
- Fu, S. Y., Q.-G. Zong, B. Wilken, and Z. Y. Pu (2001), Temporal and spatial variation of the ion composition in the ring current, *Space Sci. Rev.*, **95**, 539–554.
- Gazey, N. G. J., et al. (1996), EISCAT/CRRES observations: Nightside ionospheric ion outflow and oxygen-rich substorm injections, *Ann. Geophys.*, **14**, 1032–1043, doi:10.1007/s00585-996-1032-4.
- Glocer, A., G. Toth, and T. Gombosi (2007), Modeling ionospheric outflow during a geomagnetic storm, *AGU Fall Meeting Abstracts*, pp. B521.
- Glocer, A., G. Toth, M. Fok, T. Gombosi, and M. Liemohn (2009a), Integration of the radiation belt environment model into the space weather modeling framework, *J. Atmos. Sol. Terr. Phys.*, **71**, 1653–1663, doi:10.1016/j.jastp.2009.01.003.
- Glocer, A., G. Tóth, T. Gombosi, and D. Welling (2009b), Modeling ionospheric outflows and their impact on the magnetosphere, initial results, *J. Geophys. Res.*, **114**, A05216, doi:10.1029/2009JA014053.
- Glocer, A., G. Tóth, Y. Ma, T. Gombosi, J.-C. Zhang, and L. M. Kistler (2009c), Multifluid Block-Adaptive-Tree Solar wind Roe-type Upwind Scheme: Magnetospheric composition and dynamics during geomagnetic storms—Initial results, *J. Geophys. Res.*, **114**, A12203, doi:10.1029/2009JA014418.
- Glocer, A., N. Kitamura, G. Toth, and T. Gombosi (2012), Modeling solar zenith angle effects on the polar wind, *J. Geophys. Res.*, **117**, A04318, doi:10.1029/2011JA017136.
- Gloeckler, G., F. M. Ipavich, B. Wilken, W. Stuedemann, and D. Hovestadt (1985), First composition measurement of the bulk of the storm-time ring current (1 to 300 keV/e) with AMPTE-CCE, *Geophys. Res. Lett.*, **12**, 325–328, doi:10.1029/GL012i005p00325.
- Goldstein, J., P. Valek, D. J. McComas, and J. Redfern (2012), TWINS energetic neutral atom observations of local-time-dependent ring current anisotropy, *J. Geophys. Res.*, **117**, A11213, doi:10.1029/2012JA017804.
- Gombosi, T. I., and A. F. Nagy (1989), Time-dependent modeling of field-aligned current-generated ion transients in the polar wind, *J. Geophys. Res.*, **94**, 359–369, doi:10.1029/JA094iA01p00359.
- Gruntman, M. A., A. A. Kozochkin, and V. B. Leonas (1990), Many-electron secondary emission of thin foils bombarded by accelerated atomic beams, *Sov. J. Exp. Theor. Phys. Lett.*, **51**, 19–22.
- Hamilton, D. C., G. Gloeckler, F. M. Ipavich, B. Wilken, and W. Stuedemann (1988), Ring current development during the great geomagnetic storm of February 1986, *J. Geophys. Res.*, **93**, 14,343–14,355, doi:10.1029/JA093iA12p14343.
- Harel, M., R. A. Wolf, P. H. Reiff, R. W. Spiro, W. J. Burke, F. J. Rich, and M. Smiddy (1981), Quantitative simulation of a magnetospheric substorm. I - Model logic and overview, *J. Geophys. Res.*, **86**, 2217–2241, doi:10.1029/JA086iA04p02217.
- Hedin, A. (1992), MSIS model (1986), *Planet. Space Sci.*, **40**(4), 555–556, doi:10.1016/0032-0633(92)90209-7.
- Hedin, A. E. (1987), MSIS-86 thermospheric model, *J. Geophys. Res.*, **92**, 4649–4662, doi:10.1029/JA092iA05p04649.
- Horwitz, J. L., R. H. Comfort, P. G. Richards, M. O. Chandler, C. R. Chappell, P. Anderson, W. B. Hanson, and L. H. Brace (1990), Plasmasphere-ionosphere coupling. II - Ion composition measurements at plasmaspheric and ionospheric altitudes and comparison with modeling results, *J. Geophys. Res.*, **95**, 7949–7959, doi:10.1029/JA095iA06p07949.
- Horwitz, J. L., C. J. Pollock, T. E. Moore, W. K. Peterson, J. L. Burch, J. D. Winningham, J. D. Craven, L. A. Frank, and A. Persoon (1992),

- The polar cap environment of outflowing O(+), *J. Geophys. Res.*, **97**, 8361–8379, doi:10.1029/92JA00147.
- Ilie, R., M. W. Liemohn, J. Borovsky, and J. Kozyra (2010a), An investigation of the magnetosphere-ionosphere response to real and idealized CIR events through global MHD simulations, *Proc. R. Soc. A*, **466**(2123), 3279–3303, doi:10.1098/rspa.2010.0074.
- Ilie, R., M. W. Liemohn, and A. Ridley (2010b), The effect of smoothed solar wind inputs on global modeling results, *J. Geophys. Res.*, **115**, A01213, doi:10.1029/2009JA014443.
- Ilie, R., R. Skoug, H. Funsten, M. Liemohn, J. Bailey, and M. Gruntman (2012), The impact of geocoronal density on ring current development, *J. Atmos. Sol. Terr. Phys.*, **99**, 92–103, doi:10.1016/j.jastp.2012.03.010.
- Kozyra, J. U., V. K. Jordanova, J. E. Borovsky, M. F. Thomsen, D. J. Knipp, D. S. Evans, D. J. McComas, and T. E. Cayton (1998), Effects of a high-density plasma sheet on ring current development during the November 2–6, 1993, magnetic storm, *J. Geophys. Res.*, **103**, 26,285–26,306, doi:10.1029/98JA01964.
- Lindsay, B. G., and R. F. Stebbings (2005), Charge transfer cross sections for energetic neutral atom data analysis, *J. Geophys. Res.*, **110**, A12213, doi:10.1029/2005JA011298.
- Lu, G., P. H. Reiff, T. E. Moore, and R. A. Heelis (1992), Upflowing ionospheric ions in the auroral region, *J. Geophys. Res.*, **97**, 16,855–16,863, doi:10.1029/92JA01435.
- Lukianova, R., O. Troshichev, and G. Lu (2002), The polar cap magnetic activity indices in the southern (PCS) and northern (PCN) polar caps: Consistency and discrepancy, *Geophys. Res. Lett.*, **29**(18), 1879, doi:10.1029/2002GL015179.
- McComas, D. J., N. Buzulukova, M. G. Connors, M. A. Dayeh, J. Goldstein, H. O. Funsten, S. Fuselier, N. A. Schwadron, and P. Valek (2012), Two Wide-Angle Imaging Neutral-Atom Spectrometers and Interstellar Boundary Explorer energetic neutral atom imaging of the 5 April 2010 substorm, *J. Geophys. Res.*, **117**, A03225, doi:10.1029/2011JA017273.
- McComas, D. J., et al. (2009), The Two Wide-angle Imaging Neutral-atom Spectrometers (TWINS) NASA Mission-of-Opportunity, *Space Sci. Rev.*, **142**, 157–231, doi:10.1007/s11214-008-9467-4.
- Mitchell, D. G., P. C. Son Brandt, E. C. Roelof, D. C. Hamilton, K. C. Retterer, and S. Mende (2003), Global imaging of O⁺ from IMAGE/HENA, *Space Sci. Rev.*, **109**, 63–75, doi:10.1023/B:SPAC.0000007513.55076.00.
- Phaneuf, R. A., R. K. Janev, and M. S. Pindzola (1987), *Collisions of Carbon and Oxygen Ions With Electrons, H, H₂ and He*, Controlled Fusion Atomic Data Center, Springfield, Va.
- Powell, K. G., P. L. Roe, T. J. Linde, T. I. Gombosi, and D. L. De Zeeuw (1999), A solution-adaptive upwind scheme for ideal magnetohydrodynamics, *J. Comput. Phys.*, **154**, 284–309, doi:10.1006/jcph.1999.6299.
- Rairden, R. L., L. A. Frank, and J. D. Craven (1986), Geocoronal imaging with Dynamics Explorer, *J. Geophys. Res.*, **91**, 13,613–13,630, doi:10.1029/JA091iA12p13613.
- Ridley, A., T. Gombosi, and D. De Zeeuw (2004), Ionospheric control of the magnetosphere: Conductance, *Ann. Geophys.*, **22**, 567–584.
- Ridley, A. J., and M. W. Liemohn (2002), A model-derived storm time asymmetric ring current driven electric field description, *J. Geophys. Res.*, **107**, 1151, doi:10.1029/2001JA000051.
- Ritzau, S. M., and R. A. Baragiola (1998), Electron emission from carbon foils induced by keV ions, *Phys. Rev. B*, **58**, 2529–2538, doi:10.1103/PhysRevB.58.2529.
- Shelley, E. G., R. G. Johnson, and R. D. Sharp (1972), Satellite observations of energetic heavy ions during a geomagnetic storm, *J. Geophys. Res.*, **77**, 6104–6110, doi:10.1029/JA077i031p06104.
- Shelley, E. G., R. G. Johnson, and R. D. Sharp (1974), Morphology of energetic O⁺ in the magnetosphere, *Magnetospheric Phys. Astrophys. Space Sci. Lib.*, **44**, 135–139.
- Thomsen, M. F., J. E. Borovsky, D. J. McComas, and M. R. Collier (1998), Variability of the ring current source population, *Geophys. Res. Lett.*, **25**, 3481–3484, doi:10.1029/98GL02633.
- Tóth, G., D. L. De Zeeuw, T. I. Gombosi, and K. G. Powell (2006), A parallel explicit/implicit time stepping scheme on block-adaptive grids, *J. Comput. Phys.*, **217**, 722–758, doi:10.1016/j.jcp.2006.01.029.
- Tóth, G., D. L. De Zeeuw, T. I. Gombosi, W. B. Manchester, A. J. Ridley, I. V. Sokolov, and I. I. Roussev (2007), Sun-to-thermosphere simulation of the 28–30 October 2003 storm with the Space Weather Modeling Framework, *Space Weather*, **5**, S06003, doi:10.1029/2006SW000272.
- Tóth, G., et al. (2005), Space Weather Modeling Framework: A new tool for the space science community, *J. Geophys. Res.*, **110**, A12226, doi:10.1029/2005JA011126.
- Tóth, G., et al. (2012a), Adaptive numerical algorithms in space weather modeling, *J. Comput. Phys.*, **231**, 870–903, doi:10.1016/j.jcp.2011.02.006.
- Tóth, G., et al. (2012b), Adaptive numerical algorithms in space weather modeling, *J. Comput. Phys.*, **231**, 870–903, doi:10.1016/j.jcp.2011.02.006.
- Valek, P., J. Goldstein, D. J. McComas, R. Ilie, N. Buzulukova, M.-C. Fok, and J. D. Perez (2013), Oxygen-hydrogen differentiated observations from TWINS: The 22 July 2009 storm, *J. Geophys. Res. Space Physics*, **118**, 3377–3393, doi:10.1002/jgra.50204.
- Welling, D. T., V. K. Jordanova, S. G. Zaharia, A. Glocer, and G. Toth (2011), The effects of dynamic ionospheric outflow on the ring current, *J. Geophys. Res.*, **116**, A00J19, doi:10.1029/2010JA015642.
- Wilken, B., Q. G. Zong, I. A. Daglis, T. Doke, S. Livi, K. Maezawa, Z. Y. Pu, S. Ullaland, and T. Yamamoto (1995), Tailward flowing energetic oxygen ion bursts associated with multiple flux ropes in the distant magnetotail: GEOTail observations, *Geophys. Res. Lett.*, **22**, 3267–3270, doi:10.1029/95GL02980.
- Wing Ho, C., J. L. Horwitz, and T. E. Moore (1994), DE1 observations of polar O(+) stream bulk parameters and comparison with a model of the centrifugally-accelerated polar wind, *Geophys. Res. Lett.*, **21**, 2459–2462, doi:10.1029/94GL02340.
- Yeh, H., and J. C. Foster (1990), Storm time heavy ion outflow at mid-latitude, *J. Geophys. Res.*, **95**, 7881–7891, doi:10.1029/JA095iA06p07881.
- Young, D. T., H. Balsiger, and J. Geiss (1982), Correlations of magnetospheric ion composition with geomagnetic and solar activity, *J. Geophys. Res.*, **87**, 9077–9096, doi:10.1029/JA087iA11p09077.
- Yu, Y., and A. J. Ridley (2009), Response of the magnetosphere-ionosphere system to a sudden southward turning of interplanetary magnetic field, *J. Geophys. Res.*, **114**, A03216, doi:10.1029/2008JA013292.
- Zhang, J., et al. (2007), Solar and interplanetary sources of major geomagnetic storms during 1996–2005, *J. Geophys. Res.*, **112**, A10102, doi:10.1029/2007JA012321.
- Zheng, Y., A. T. Y. Lui, and M.-C. Fok (2008), Viewing perspective in energetic neutral atom intensity, *J. Geophys. Res.*, **113**, A09217, doi:10.1029/2008JA013070.